Shortwave Radiative Effect of Arctic Low-Level Clouds: Evaluation of Imagery-Derived Irradiance with Aircraft Observations

Hong Chen[1,2], Sebastian Schmidt[1,2], Michael D. King[2], Galina Wind[3], Anthony Bucholtz[4], Elizabeth A. Reid[4], Michal Segal-Rozenhaimer[5,6,7], William L. Smith[8], Patrick C. Taylor[8], Seiji Kato[8], Peter Pilewskie[1,2]

5   [1]University of Colorado, Department of Atmospheric and Oceanic Sciences, Boulder, CO, USA
[2]University of Colorado, Laboratory for Atmospheric and Space Physics, Boulder, CO, USA
[3]Science Systems and Applications, Inc., Lanham, MD, USA
[4]Naval Research Lab, Monterey, CA, USA
[5]Bay Area Environmental Research Institute Sonoma, Sonoma, CA, USA
10   [6]NASA Ames Research Center, Moffett Field, CA, USA
[7]Department of Geophysics, Porter School of the Environment and Earth Sciences, Tel-Aviv University, Israel
[8]NASA Langley Research Center, Climate Science Branch, Hampton, VA, USA

Correspondence to: Sebastian Schmidt (sebastian.schmidt@lasp.colorado.edu)

Abstract. Cloud optical properties such as optical thickness along with surface albedo are important inputs for deriving the shortwave radiative effects of clouds from space-borne remote sensing. Owing to insufficient knowledge about the snow or ice surface in the Arctic, cloud detection and the retrieval products derived from passive remote sensing, such as from the Moderate Resolution Imaging Spectroradiometer (MODIS), are difficult to obtain with adequate accuracy – especially for low-level thin
5 clouds, which are ubiquitous in the Arctic. This study aims at evaluating the spectral and broadband irradiance calculated from MODIS-derived cloud properties in the Arctic using aircraft measurements collected during the Arctic Radiation-IceBridge Sea and Ice Experiment (ARISE), specifically using the upwelling and downwelling shortwave spectral and broadband irradiance measured by the Solar Spectral Flux Radiometer (SSFR) and the BroadBand Radiometer system (BBR). This entails the derivation of surface albedo from SSFR/BBR and camera imagery for heterogeneous surfaces in the marginal ice zone (MIZ), as well as
10 subsequent measurement-model inter-comparisons in the presence of thin clouds. In addition to MODIS cloud retrievals and surface albedo from SSFR, we used temperature and humidity data from in-situ data and reanalysis (MERRA-2).

       The spectral surface albedo derived from the airborne radiometers is consistent with prior ground-based measurements, and adequately represents the surface variability for the study region and time period. Somewhat surprisingly, the primary error in MODIS-derived irradiance fields for this study stems from undetected clouds, rather than from the retrieved cloud properties. In
15 our case studies, about 22% of clouds remained undetected (cloud optical thickness less than 0.5). The radiative effect of clouds above the detection threshold was -40 Wm^{-2} above cloud, and -39 Wm^{-2} below the cloud layer, and the optical thickness from the MODIS "1621" cloud product was consistent with the reflected and transmitted irradiance observations.

       This study suggests that passive imagery cloud detection could be improved through a multi-pixel approach, that would make it more dependable in the Arctic. Regardless of the cloud retrieval method, there is a need for an operational imagery-based
20 surface albedo product for the polar regions that adequately captures its temporal, spatial, and spectral variability to estimate cloud radiative effect from space-borne remote sensing.

1 Introduction

Understanding the warming of the Arctic necessitates an understanding of the radiative impact of clouds, surface albedo, and water vapor, especially at the surface where the interaction with the cryosphere occurs (Curry et al., 1996; Shupe and Intrieri, 2004). Clouds cool the surface in the shortwave (SW) wavelength range by reflecting solar radiation and warm the surface in the longwave (LW). Low-level, liquid-bearing clouds have recently received special attention because they significantly contributed to the 2012 enhanced Greenland ice melt (Bennartz et al., 2013). When they are optically thin (LWP smaller than 20 gm^{-2}), their SW cooling effect is small because they do not reflect much sunlight, especially when the surface is already bright. In the LW, on the other hand, their emissivity increases rapidly with the liquid water path (LWP), making them blackbodies and warm the surface especially if they are at a low altitude. For larger LWP, the SW cooling eventually dominates as the cloud becomes more reflective.

Valuable data on Arctic clouds has been collected by ground-based observations over the past few decades (Curry et al., 1996, Shupe et al., 2011), but they are limited in spatial coverage and needed to be augmented by additional observations, especially from space-borne remote sensing measurements to help gain meaningful insights of cloud radiative effects in the Arctic as a whole.

Hartmann and Ceppi (2014) used the dataset from the Clouds and the Earth's Radiant Energy System (CERES) and showed that every 10^6 km^2 decrease in September sea ice extent is associated with a 2.5 Wm^{-2} increase in annual-mean absorbed solar radiation. Kay and L'Ecuyer (2013) used combined products from active and passive remote sensing and showed that during the 2007 summer, the cloud reduction and sea ice loss in the Arctic resulted in more than 20 Wm^{-2} anomalies in shortwave radiation at the top of the atmosphere (TOA). The radiation products used in these studies, e.g., CERES-EBAF (Loeb et al., 2012), 2B-FLXHR-LIDAR (Henderson et al., 2013), all rely on coincident cloud observations from the Moderate Resolution Imaging Spectroradiometer (MODIS).

MODIS is a 36-band passive imager onboard the Terra and Aqua satellites. It provides cloud optical parameters (COPs), e.g., cloud optical thickness (COT), cloud effective radius (CER), and cloud thermodynamic phase, from which irradiance can be derived. The COPs from MODIS have been used extensively in studies of cloud radiative effects (e.g., Wielicki et al., 1996; Platnick et al., 2003; Loeb and Manalo-Smith, 2005; Oreopoulos et al., 2016). Due to the lack of temperature and reflectance contrast between clouds and the underlying surface in the Arctic, detecting the clouds is challenging for passive remote sensing, especially when they are thin and occur at a low level. Liu et al. (2010) showed that the MODIS cloud detection algorithm performs better over the ocean than over the ice. The traditional cloud retrieval algorithm (Nakajima and King, 1990) retrieves COT and CER from the reflectance at two channels, one where clouds do not absorb (660, 860, or 1240 nm), and one where cloud drops are weakly absorbing (1630 or 2130 nm). Over snow and ice, the surface albedo is already high in the visible and near-infrared (leaving little dynamic range for cloud remote sensing of optical thickness) and varies regionally and temporally (leading to uncertainties in the retrieval products). This, in combination with low-sun conditions, makes it difficult to obtain accurate cloud optical properties from passive remote sensing. To improve the reliability of MODIS cloud retrievals in the Arctic, an algorithm has been developed that uses two shortwave-infrared bands of 1630 nm and 2130 nm, where snow and ice are relatively dark (Platnick et al., 2001; King et al., 2004). However, the surface albedo varies with surface type even for these bands, and the operational algorithm assumes constant values obtained from a climatology based on 5 years of Terra/MODIS data (Moody et al., 2007).

In addition to the COPs themselves, the snow/ice surface albedo also plays an important role in determining the cloud radiative effect and radiation energy budget in the Arctic (Shupe and Intrieri, 2004). The surface albedo changes significantly from the visible to the near-infrared wavelength range (Wiscombe and Warren, 1981; Brandt et al., 2005) with different spectral dependence depending on the surface conditions (e.g., snow and ice). Inhomogeneous surface conditions such as floes of partially snow-covered ice, varying snow depth and snow grain size, and surface topography (e.g., sastrugi), all affect the spectral shape and magnitude of the surface albedo. Its variability is poorly understood due to insufficient knowledge about the Arctic surface.

Spectral surface albedo measurements for snow and ice have been collected during ground-based field experiments in polar regions (e.g., Perovich et al., 2002; Brandt et al., 2005). However, they do not necessarily capture the spatial and temporal variability in the Arctic surface conditions.

Finally, water vapor, the most abundant natural greenhouse gas, plays a key role in modulating the surface radiation
5   budget (Schmidt et al., 2010). In the Arctic, water vapor has a special significance due to frequent temperature inversions, complex cloud regimes, and moisture advection (Curry et al., 1995). Doyle et al. (2011) showed that an average of 17 Wm^{-2} increase in downwelling longwave irradiance (LWD) was associated with a moisture intrusion during 9-11 February 2010, on Ellesmere Island in the Canadian High Arctic, and that optically thin clouds further increased LWD by 20 Wm^{-2}. Sedlar and Devasthale (2012) showed that the water vapor anomaly positively covaries with temperature anomaly, resulting in an anomaly as large as ±10 Wm^{-2}
10   in clear-sky LWD. Without adequate information, the varying water vapor content in the Arctic atmosphere can contribute to uncertainties in radiative calculations.

In summary, the challenges for deriving CRE from passive remote sensing are (a) inaccurate detection of clouds and cloud optical property retrievals over snow or ice surfaces; (b) lack of accurate surface albedo as a constraint in the radiative transfer model (RTM); (c) insufficient knowledge about the water vapor content.
15   The aim of this paper is to use aircraft radiation measurements collected during the NASA Arctic Radiation – IceBridge Sea & Ice Experiment (ARISE, Smith et al., 2017) to evaluate irradiance as derived from coincident satellite imagery, and to investigate the causes of any biases. In the first step, the spectral snow surface albedo was derived from upwelling and downwelling irradiance measurements, accounting for partially snow-covered scenes by the snow fraction estimated from aircraft camera imagery. In the second step, we used an RTM to calculate the upwelling and downwelling broadband and spectral irradiance at flight
20   level, incorporating the MODIS-derived COPs and spectral surface albedo derived from the aircraft measurements as inputs.

The calculated irradiances were then compared with the measured broadband and spectral irradiance pixel by pixel for two cases – above-cloud and below-cloud. Section 2 describes the data and method used in this study. Section 3 provides the results and discussions for the measured spectral surface albedo, as well as for the comparisons between irradiance calculations and measurements. Conclusions are drawn in Section 4.

25   **2 Data and Methods**

ARISE was a NASA airborne measurement campaign to study snow and ice properties in the Arctic marginal ice zone (MIZ) in conjunction with cloud microphysics and radiation (Smith et al., 2017). The NASA C-130 aircraft was instrumented with shortwave and longwave radiometers, described in this section, along with cloud microphysics probes, aerosol optical properties instruments, and snow and ice remote sensors. The experiment was based at Eielson Air Force Base near Fairbanks, Alaska, from 2 September
30   to 2 October 2014, to capture the September sea ice minimum. One of the primary objectives of ARISE was to validate irradiance (or flux densities) derived from CERES-MODIS observations with aircraft radiation measurements.

In this paper, we use imagery from a downward-looking video camera together with measurements of shortwave broadband and spectral irradiance. In the Arctic, overpasses of polar-orbiting satellites are fairly common. ARISE targeted multiple overpasses of MODIS and CERES on Aqua, Terra, or VIIRS on Suomi NPP on almost every flight. We focus on two science
35   flights on 11 September and 13 September that sampled under above- and below-cloud conditions, respectively. These flights include so-called "lawnmower" patterns, a series of parallel flight legs laterally offset by about 20 km as shown in Fig. 1. They were specifically designed for ARISE to sample one or two 100×100 km^2 grid boxes per flight with sufficient coincident CERES

footprints (each with a 20-km diameter at nadir) to acquire statistically significant above- or below-cloud aircraft measurements for the validation of CERES-MODIS derived irradiance.

Comparing the aggregated data from ARISE directly with the CERES-MODIS flux products within the grid box, e.g., using histograms, is challenging because of the heterogeneity of the scenes in terms of surface albedo, cloud conditions, and changing solar zenith angle. Therefore, we instead compare satellite-based radiative transfer calculations and aircraft observations pixel by pixel along the flight track. We use the MODIS cloud products (see Section 2.4) from collection 6.1 instead of CERES fluxes because of their higher spatial resolution (1 km versus 20 km). From these cloud products, above- and below-cloud spectral and broadband irradiance are calculated, with the additional input of spectral surface albedo derived from ARISE aircraft measurements. The details of each dataset and instrument are described in the following subsections.

2.1 BroadBand Radiometer System (BBR)

The BBRs deployed during ARISE are modified CM 22 Precision Pyranometers from Kipp & Zonen (Bucholtz et al., 2010). They measured upwelling and downwelling broadband irradiance (unit: W m^{-2}) that is, the spectrally integrated irradiance from 200 nm to 3600 nm. In addition, a sunshine pyranometer (SPN-1) was flown to measure diffuse and global radiative fluxes (Badosa et al., 2014; Long et al., 2010). The SPN-1 radiometer was originally intended for ground-based use, but is suited for airborne measurements of global and diffuse radiative fluxes because it does not have any moving parts, unlike traditional instruments such as the Multifilter Rotating Shadowband Radiometer (MFRSR).

2.2 Solar Spectral Flux Radiometer (SSFR)

To attribute discrepancies between satellite-derived irradiance and airborne observations to causes such as erroneous water vapor, cloud properties, or three-dimensional radiative transfer effects, spectrally resolved measurements are needed (Schmidt and Pilewskie, 2012). SSFR is a moderate resolution flux spectrometer built at the Laboratory for Atmospheric and Space Physics (LASP, University of Colorado Boulder). It is an updated version of the heritage spectrometer system originally developed at NASA Ames (Pilewskie et al., 2003).

SSFR is typically flown in conjunction with an Active Leveling Platform (ALP, also built at LASP), which was originally developed for the ER-2 and was re-built for the C-130. Counteracting the changing aircraft attitude with a system that keeps the zenith light collector horizontally aligned is particularly important in the Arctic, where low sun elevations lead to large systematic errors for fix-mounted or poorly stabilized sensors (Wendisch et al., 2001). One reason is that radiation from the lower hemisphere (for example, from clouds below or at the aircraft altitude) is registered by the zenith detector when it is tilted, which leads to systematic biases that cannot be corrected. Another reason lies in the specific design of the SSFR light collectors, which are realized as integrating spheres with a circular aperture on top. They diffuse the incoming light collected by the aperture and bundle it into a fiber optics cable that transmits it to the spectrometer system inside the aircraft (Schmidt and Pilewskie, 2012). The integrating sphere has an imperfect response to the incidence angle θ (Kindel, 2010), in contrast to the response of broadband radiometers such as BBR, which are closer to $\cos(\theta)$ as required for irradiance. At high sun elevations, a so-called hot spot arises from a baffle that prevents light from being directly transmitted into the fiber optics. Since the response deviates significantly from the 1:1 line, the direct and the diffuse light need to be corrected differently. The diffuse/direct correction is done by separating the diffuse and direct component from spectral radiative transfer calculations based on broadband SPN-1 measurements (details are provided in Appendix A), and further assuming that the downwelling diffuse radiation is close to isotropic. This assumption becomes invalid if parts of the lower hemisphere are in the light collector's field of view.

The light collector's angular response to the azimuthal angle also needs to be considered. Throughout the course of the mission, the zenith light collector revealed a response that depended on the relative azimuth of the sun to the aircraft, which was characterized by two calibration circles flown on 2 October. The non-homogeneous azimuthal response of the zenith light collector occurred for solar zenith angles greater than 66°. In many cases, an azimuthally variable response (i.e., a signal that depends on either the sun azimuth angle or on aircraft heading angle) can be attributed to the tail and/or propellers of the host aircraft. BBR and SPN-1, which were both fix-mounted on the C-130, would also be affected. To assess their azimuthal response, the attitude-corrected BBR data (Bannehr and Schwiesow, 1993; Bucholtz et al., 2008; Long et al., 2010) was compared with the SPN-1 global irradiance data, as well as with radiative transfer calculations. This comparison revealed that in this case, aircraft interferences were actually minor compared to atmospheric effects. Only SSFR measurements, but not BBR and SPN-1, had a significant azimuthal dependence, suggesting the SSFR light collector as the source, rather than aircraft interferences. To determine the SSFR azimuthal response during the mission, SSFR's measurements were referenced to BBR during a full calibration circle flown on 2 October (details are provided in Appendix B). The calibration circle constitutes SSFR's azimuthal response at this solar zenith angle, which was then used to correct SSFR's downwelling irradiance for the conditions encountered for the SSFR data collected during other research flights. By using BBR, SPN-1, and SSFR in such a way, the redundancies between the instruments were used to capitalize on the strengths of the individual instruments (BBR: un-biased angular response; SPN-1: diffuse/global separation; SSFR; spectral resolution for sub-range of BBR and SPN-1).

In addition to the angular calibrations, wavelength and radiometric calibrations were performed in the laboratory before and after the mission. The wavelength calibrations ensured spectral accuracy by referencing the SSFR measurements to several line sources. The primary radiometric calibration, performed with a NIST-traceable calibrated lamp, links SSFR measured digital counts to spectral irradiance. In addition, the radiometric calibration was transferred to a so-called secondary radiometric field standard, which monitored the stability of the radiometers throughout the mission. From the SSFR measurements, spectral albedo, net flux, and absorption can be derived at a spectral resolution of 8-12 nm (4-6 nm sampling). From the spectral albedo, cloud optical properties or surface albedo can be derived. To increase signal-to-noise ratio, spectral or spatial binning is possible. A spatial data aggregation technique is pursued here (Section 3.1).

2.3 Imagery from Downward-Looking Video Camera

A downward-looking video camera (referred to as "nadir camera") is often included as a standard payload on NASA aircraft. It typically records scenes for context only and is not radiometrically or geometrically calibrated. Despite this shortcoming, the videos recorded by the nadir camera are used for quantitative image analysis. From the video, we first extract image frames with an average rate of 2 Hz (2 frames per second). To co-register the nadir imagery in conjunction with the measurements from other instruments, the times for individual image frames are also needed. However, the image frames themselves did not contain a digitally stored time. Instead, they included a timestamp located at the lower left side that contains time information. We used Optical Character Recognition (OCR) to retrieve the time from this information.

In the second step, the nadir camera imagery was used to quantify the fractional snow coverage. The snow fraction was estimated by calculating the fraction of bright pixels of the image. To this end, the image was converted from RGB (red, green, and blue) into grayscale through

$$Gray = 0.299R + 0.587G + 0.114B \tag{1}$$

for each pixel. One issue of the nadir camera imagery was the darkening effect from the center to the edge of its field of view, which is known as the vignette effect. To compensate, the brightness of the image was linearly increased from edge to center through an image blending and interpolation technique by Haeberli and Voorhies (1994):

$$out = (1 - \beta) \times Black + \beta \times Gray \qquad (2)$$

5 where $Black$ is a black image with the same dimensions as Gray, and β is the image blending factor, a 2D matrix with increasing values of 1.1-1.5 from the image center to the edge. The operator "×" denotes element-by-element multiplication. To avoid the vignetting extremes in the corners, only the imagery within a circle centered on the image was used to derive snow fraction (left panel of Fig. 2a). The key step of the snow fraction detection algorithm is the separation of dark versus bright pixels. An adaptive thresholding technique was applied to estimate the snow fraction. The adaptive thresholding is an approach for handling an image

10 with unevenly distributed intensities by dividing the image into subimages and assigning different thresholds for each of the subimages (Gonzalez et al., 2002). The details of the adaptive thresholding are described in Appendix C. The snow fraction is estimated by

$$Frac = \frac{N_{bright}}{N_{total}} \qquad (3)$$

where N_{bright} is the number of thresholding pixels and N_{total} is the total number of pixels within the circle. The detection results

15 for the left panel in Fig. 2a are illustrated in the right panel. The method provides robust estimates of snow fraction from the nadir downward-looking imagery, even for scenes with pure snow. Figure 2b shows the simultaneously measured upwelling and downwelling spectral flux from the SSFR for the scene shown in Fig. 2a.

2.4 C-130 Thermometer and Hygrometer and Modern-Era Retrospective analysis for Research and Applications version 2 (MERRA-2)

20 The NASA C-130 aircraft was equipped with a thermometer and a hygrometer to measure air temperature and relative humidity. Figure 3b shows the profiles derived from C-130 during a descending leg from 19:31:14 (altitude: 6.447 km) to 19:50:05 (altitude: 0.258 km) on 13 September, 2014. Due to a malfunction of the hygrometer on 11 September, 2014, no profile from C-130 is available on this day. Instead (Figure 3a), we use the temperature and water vapor content profiles from MERRA-2, which is an atmospheric reanalysis dataset from NASA (Bosilovich et. al., 2015). MERRA-2 (M2I3NVASM) provides 3-hourly assimilated

25 3D meteorological fields (dimensions: 576 in longitude; 361 in latitude; 72 pressure levels from 985 hPa to 0.01 hPa). The comparison of in-situ profiles and MERRA-2 in Figure 3b shows good agreement, although the reanalysis does not reproduce the details of the vertical profile. A more systematic comparison of reanalysis and in-situ data from ARISE is done by Rozenhaimer et al. (2018) and is not the focus of this paper. The observations reveal much drier and slightly colder conditions than captured in the widely used subarctic climatology from Anderson et al. (1986), referred to here as AFGL. Above 6.5 km, we used the clima-

30 tology regardless to provide complete temperature and water vapor profiles from 0 to 120 km, after rescaling them to the observed temperature and water vapor values at 6.5 km.

2.5 Moderate Resolution Imaging Spectroradiometer (MODIS)

The publicly available pixel-level MODIS cloud products (MOD/MYD06, collection 6.1), which are provided in 5-minute granules, are used in this study (Platnick et al., 2017). The MODIS cloud product includes COPs such as COT, CER, and cloud thermody-

35 namic phase, which are essential parameters for calculating cloud radiative effects. As described before, the MODIS COT and

CER are retrieved simultaneously using a bi-spectral reflectance method (Nakajima and King, 1990). To minimize the influence of the surface on cloud retrievals, the 1630 nm and 2130 nm bands are used since the snow and ice surface are relatively dark at those two bands (Platnick et al., 2001; King et al., 2004). These retrievals are included in the MOD/MYD06 files and will be referred to as the "1621" cloud product. Since the clouds evaluated in this study are all liquid, the cloud thermodynamic phase is

5   not assessed. The data include COPs for cloudy and partially cloudy conditions (the latter are indicated by "PCL" in the MODIS data variable name), as described in Platnick et al. (2017).

The MODIS "1621" cloud product was extracted over the flight track and then input into a radiative transfer model (RTM) to calculate spectral and broadband irradiance at flight level. A 1-D RTM (libRadtran version 2.0.1, Emde et al., 2016) was used for radiative transfer calculations in this paper. The RTM uses

10   1)   Day of the year (for accurate Sun-Earth distance);

      2)   Atmospheric profile; here, the subarctic summer atmospheric profile from Anderson et al. (1986);

      3)   Water vapor content profile from MERRA-2 for 11 September and from C-130 thermometer for 13 September, 2014;

      4)   Temperature profile from MERRA-2 for 11 September and from C-130 hygrometer for 13 September, 2014;

      5)   Solar zenith angle;

15   6)   Wavelength;

      7)   Surface albedo at the specified wavelength;

      8)   Slit functions (also known as instrument line shape), which describe the bandpass function of the spectrometer; here, SSFR slit functions as measured in the laboratory are used

      9)   Cloud layer altitudes, cloud optical thickness, and cloud effective radius; here, MODIS-COPs;

20   10)   Phase functions; here, from Mie calculations distributed with libRadtran;

      11)   Output altitude; here flight altitude.

The RTM uses a solar spectrum with 1 nm resolution as solar source at TOA (Kurucz, 1992). The Discrete Ordinates Radiative Transfer Program (DISORT, Stamnes et al, 1988) is used as the radiative transfer solver. LOWTRAN 7 (Pierluissi and Peng, 1985) is used for the molecular absorption parameterization. The RTM output includes downwelling (global and direct) and upwelling

25   irradiance at specified output altitude and wavelength. The output altitude is set to flight altitude. The wavelength range of the calculations is set to 200 to 3600 nm.

3. Results and Discussions

This section shows the results for the mixed-scene spectral surface albedo derived from SSFR, and the comparisons of broadband and spectral irradiance between aircraft measurements and MODIS-COP based radiative transfer calculations (referred to as "cal-

30   culations").

3.1 Spectral Surface Albedo

The spectral surface albedo results shown in this subsection stem from the aircraft measurements from 20:00:26 UTC to 20:10:51 UTC on 13 September. Only the SSFR measurements under clear-sky (no clouds above or below) scenes above snow or ice, as identified from the forward and nadir cameras, were used to calculate the spectral flight level albedo through

35   $Albedo = \frac{F(\lambda)^{\uparrow}}{F(\lambda)^{\downarrow}}$ (4)

where $F(\lambda)^{\uparrow}$ and $F(\lambda)^{\downarrow}$ are SSFR-measured spectral upwelling and downwelling irradiance. An atmospheric correction was applied to the flight level albedo calculated from Equation (4) using RTM and the atmospheric profiles derived in Section 2.4. This was done through RT calculations with five surface albedo spectra: the measured flight level albedo from SSFR, α_{SSFR}, scaled by 0.6, 0.7, 0.8, 0.9, and 1.0. The five α_{SSFR} and RTM calculations provided a modeled relationship for surface and flight level albedo
5 (nearly linear). The linear relationship at each wavelength was then inverted to infer the surface albedo from the measurements at flight level. To capture the spatial and spectral variability of the surface, we developed a data aggregation technique that combines collective measurements in a partially snow-covered environment into one spectral surface albedo dataset that is parameterized by snow fraction ("binary" representation of the radiative surface properties), which is estimated from the nadir camera imagery using the method described in Section 2.3. Each surface albedo data point was linked to the associated snow fraction. From the collection
10 of data points, the relationship between the spectral surface albedo and snow fraction can be investigated.

The SSFR wavelengths at water absorption bands, and those less than 350 nm or greater than 1800 nm, were excluded from the albedo data set because of a low signal-to-noise ratio. Figure 4 shows the surface albedo at 640 nm, 1240 nm, and 1630 nm plotted versus the snow fraction. Linear regression can be used to establish a simple relationship between snow fraction and albedo, assuming that each observed spectrum is a mixture of only two so-called end-members: the spectral albedos of a dark and
15 a bright surface. These end-members can vary depending on the local conditions. For example, the dark component can either be open ocean or young ice. The bright component can either be thick ice or a snow-covered surface. The resulting spectral surface albedo for a mixed sampling region is established through the slopes and intercepts of the linear fit, with the snow fraction ranging from 0 to 1 as the independent variable. The representative snow albedo for the region at a particular wavelength can be read off on the right side of Fig. 4 (snow fraction of 1). This simple separation method has obvious drawbacks; for example, the implicit
20 linear-mixing assumption, the variability of the end-members, and data sparsity of the individual end members (in the example in Fig. 4, snow fractions below 0.6 rarely occur). However, it is the most effective way to characterize mixed regions, which are the norm for the MIZ.

The snow spectral end-member (snow fraction of 1) of the mixed-scene spectral surface albedo (referred to as "2013-09-13 surface albedo") is shown in Fig. 5. As expected, the surface albedo is high in the shortwave range from 400 to 900 nm and
25 decreases in the near-infrared. The SSFR-derived albedo spectra resembles the ground-based measurements of thick snow over ice near Davis Station, Antarctica (Brandt et al., 2005), and is fairly consistent with the dry-season climatology (Kay and L'Ecuyer, 2013) except at 1200 nm where spring-time aircraft measurements near Barrow (Alaska, Lyapustin et al., 2010) are closer. Overall, the data sets differ significantly in the visible wavelength range.

Figure 5 also shows the surface albedo with zero snow fraction. As pointed out above, snow fractions below 0.6 were
30 extremely rare during 20:00:26 UTC - 20:10:51 UTC on 13 September. Nevertheless, the mixed-surface data, extrapolated to 0 snow fraction, compares surprisingly well to ground-based measurements of young gray ice, taken during the Australian National Antarctic Research Expeditions (ANARE) in 1996 (Warren et al., 1997). This suggests that during the sampled time period, the dark pixels from the nadir camera imagery are dominated by various freezing states.

As mentioned above, the binary representation of surface types oversimplifies the actual mixture of ice at different freez-
35 ing stages, but is adequate to serve as surface albedo input for the RTM to constrain the irradiance calculations over mixed surfaces in the next subsections.

3.2 Broadband Irradiance Comparison

In this section, we show broadband irradiance comparisons between SSFR and BBR measurements and MODIS-COPs based RTM calculations at aircraft flight level for an above-cloud case and a below-cloud case, collected by the research flights on 11 September and 13 September, respectively.

5   The RTM irradiances were calculated for wavelengths from 200 nm to 3600 nm. Since the SSFR-derived surface albedo described in previous subsection was not available at wavelengths shorter than 350 nm, gas absorption bands, and wavelengths greater than 1800 nm due to a low signal-to-noise ratio, several techniques were applied to fill in the surface albedo spectra. Figure 6 is an illustration of how the surface albedo was calculated for 11 September. First, the "13 September surface albedo" (Section 3.1) with a constant snow fraction of 70% is calculated from the linear regression coefficients (marked in red). This is justified

10 because this flight occurred in a similar geographical area. In the gas absorption bands (red area), the surface albedo was replaced with interpolated values; from 1800nm to 1900nm, a polynomial fit was used for extrapolation, based on the spectral dependence from 1650 nm to 1800 nm. For the wavelengths shorter than 350 nm and greater than 1900 nm, we used modeled snow albedo (Wiscombe and Warren, 1981) times a scale factor to match the measurements at the joinder wavelength.

    Figure 7 and Fig. 8 show the broadband irradiances from SSFR, BBR, and the calculations (Fig. 7a: downwelling; Fig.

15 7b: upwelling) for the above-cloud case, where the aircraft was flying at an altitude around 7 km. After applying the azimuthal correction, the SSFR downwelling irradiance measurements agree with those from BBR. The observed variability in the downwelling signal is due to the occurrence of cirrus above the aircraft, which is confirmed by the forward camera. For the upwelling irradiance, the MODIS-derived baseline value of 230 Wm^{-2} corresponds to locations where MODIS did not detect any clouds. It is important to note that the value of the baseline indicates the RTM calculations under clear-sky condition, which would change

20 if a different surface albedo parameterization or a different snow fraction were used. For a snow fraction of 0.7 in the "13 September surface albedo" parametrization, the calculations agree with the measurements within 10%. The optical thickness along the flight track (included in Fig 7b) ranges from 0.5 to 15.3, with a median of 5.7, suggesting that MODIS does not retrieve clouds with an optical thickness below 0.5. In contrast to the calculations, the measurements show a continuous variation from leg to leg, suggesting that the clouds actually extended beyond the locations where MODIS detected them. To confirm, a sequence of nadir camera

25 imagery (Fig. 7b i - iv) is interpreted. At close inspection, it shows wave patterns, suggesting the existence of thin clouds in regions where MODIS does not detect any. In this case, undetected optically thin clouds made up almost one fifth of the points along the flight track. Fig. 7b indicates that the undetected clouds lead to an underestimation of the upwelling irradiance by 30 Wm^{-2} averaged over these pixels (>10% discrepancy). By contrast, the calculated irradiances for the locations where MODIS does detect clouds are only 10 Wm^{-2} lower than the measurements (4%), which is only slightly larger than the BBR/SSFR measurement uncertainty

30 and can be explained either by (a) incorrect COPs (optical thickness, effective radius, or thermodynamic phase) and/or (b) inaccurate or variable surface albedo. To quantify the contributions of these effects to the total discrepancy, the spectral information from SSFR is used in the next section.

    After the investigation of the above-cloud case for MODIS-derived irradiance, we turn our attention to the below-cloud case, which relates to near-surface irradiance. The primary cloud layer consisted of stratocumulus cloud and was located between

35 0.8 and 1.2 km. A secondary cloud layer close to the surface, located below the aircraft's minimum flight altitude of 500 ft (approximately 150 m), frequently occurs due to a temperature inversion close to the surface, where leads and cracks in the ice provide the necessary moisture for their formation. These clouds also need to be considered to quantify the radiative surface budget, but they are excluded from the analysis here because the aircraft could not underfly them. As a result, only the data from 22:21:00 to 22:25:48 (minimal occurrence of the secondary cloud layer as indicated by the forward and nadir camera imagery) was selected

40 for comparison. In contrast to the above-cloud case where the surface albedo was held constant in the RTM, the surface albedo

variability on the below-cloud leg was considered here. The missing wavelengths were filled in as illustrated in Fig. 6. Deriving the surface albedo directly from the measurements was impossible because the zenith irradiance varied due to the overhead cloud layer. Instead, it was obtained from the ARISE parameterization via the snow fraction, derived from the nadir camera imagery for each point along the leg (see Section 3.1). Figure 8 shows the upwelling and downwelling broadband irradiance comparison be-

5 tween calculations and observations from BBR and SSFR. When incorporating the "13 September surface albedo" into the RTM, the upwelling irradiance calculations resemble the SSFR and BBR measurements (Fig. 8b). The calculations agreed well with SSFR and BBR when clouds were detected except for the time period before 22:22:48 when the aircraft was entering the cloud field. The MODIS granule from Aqua was a snapshot of the cloud scene at 22:10, 10 minutes prior to the beginning of the flight leg. Measurement-model discrepancies for specific pixels can therefore be explained by changes of the cloud field over time. The

10 bimodal behavior that is apparent in the time series (Fig. 8a and 8b) as well as in the histograms (Fig. 8c) stems from time periods with and without clouds in the model input. The observations show no evidence of any cloud gap – hence only one mode appears. From the distance of the cloudy/clear modes, one can estimate the pixel-level bias caused by undetected clouds: 45 Wm^{-2} bias for the downwelling and 19 Wm^{-2} bias for the upwelling shortwave irradiance. One can also estimate the cloud radiative effect (CRE, provided in Table 1 and 2 for 11 September and 13 September) from the difference of the net irradiance between the calculations

15 when clouds are detected and when they are not detected (clear-sky).

3.3 Spectral Irradiance Comparison

Although the model-measurement biases in the broadband shortwave CRE are negligible when clouds were detected, the time series as shown in Fig. 7b do not quite match, especially for the thin parts of the clouds near the edge of a field. To diagnose the

20 cause, we use the spectrally resolved measurements by SSFR in this section.

For the above-cloud case (11 September), Fig. 9 presents the spectral irradiance comparison at 860nm and 1640nm. To put these results into context, the RTM calculations (based on "13 September surface albedo" with SF=70%) were also performed with climatological surface albedos of the Arctic dry and wet seasons (0.85 and 0.75) for 860nm from Kay and L'Ecuyer (2013). As shown in Fig. 9a, the baseline of the clear-sky RTM calculations varied significantly with surface albedo. Arctic dry-season

25 surface albedo is clearly inconsistent with the conditions during the flight; instead the measurements support a surface albedo somewhere between the ARISE parameterization and the wet-season climatology value. These results reveal the importance of the spectral surface albedo since any inaccuracies will propagate into model biases for both cloudy and clear-sky conditions. The irradiance range apparent in the time series varies considerably with surface albedo; the climatology surface albedos result in a much smaller range than obtained from the measured surface albedo. Consequently, the clouds' shortwave cooling effect might be

30 underestimated by some climate models. In this context, it is important to note that the small broadband model-measurement discrepancy of 8 Wm^{-2} from Fig. 6) is only achieved when the SSFR derived surface albedo is used in the RTM calculations; otherwise it would be larger. At 1640nm (Fig. 9b), there is excellent model-measurement agreement for the clear-sky baseline and for cloudy pixels that MODIS detects. This is because snow is dark in the shortwave infrared, and because MODIS COPs in the Arctic are primarily based on these wavelengths. Because of the obvious distinction between cloudy and clear pixels in the meas-

35 urements and calculations, it is possible to estimate the fraction of partially or fully cloudy pixels that are not detected by MODIS. Of all pixels along the flight leg with a MODIS-COD below the detection threshold of 0.5 (i.e., "clear"), 22% (highlighted in green) are actually cloudy. One interesting finding from the broadband irradiance comparison (Fig. 6b) is that the calculations are low-biased relative to the observations. However, from the spectral comparison (Fig. 9), the calculations have larger/similar values than

the SSFR measurements at 860 nm/1640 nm. To reconcile the apparently contradictory results, we use the full spectrum from the calculations and observations at 21:24 UTC on 11 September, when the broadband calculation indicates a 6 Wm^{-2} low bias.

Figures 10a and 10b show the spectral upwelling irradiance from the RTM calculations and from the SSFR measurements, as well as the ratio of RTM and SSFR. The agreement in the water vapor absorption bands indicates that MERRA-2 is sufficient

5 to prescribe the water vapor content in the calculations. Outside of the gas absorption bands, the calculations agree with the measurements at wavelengths smaller than around 850nm, but are slightly low-biased at near-infrared wavelengths. Spectral discrepancies are caused by the use of inaccurate 1) surface albedo 2) cloud optical parameters, some of which compensate each other in the broadband integral. Such error compensation may lead to an improved model-measurements agreement for the "wrong reasons"; therefore, validation efforts should include spectrally resolved measurements.

10 So far, the analysis did not reveal whether the observed model-measurement discrepancies are due to biases in the COPs or in the surface albedo. Figures 11-12 are an attempt to disentangle both sources of uncertainty despite the limited number of observations during ARISE. Figure 11 shows the ratio between modeled (labeled "RTM") and measured ("SSFR") upwelling broadband irradiance at flight-level as a function of the retrieved COT for the collection of cloudy pixels from 11 September. At large COT, clouds dominate the upwelling irradiance, whereas the surface dominates in the limit of zero COT (as stated above, the

15 retrieved minimum is 0.5). The ratio of RTM/SSFR can be used to indicate how biased the surface albedo is in the RTM when COT is approaching to 0 and how biased the cloud optical properties are when the COT approaches large values. The data reveal a functional relationship between COT and the RTM/SSFR ratio. An exponential fitting of $y = a - e^{bx+c}$ is used to parameterize the upwelling irradiance ratio as a function of COT. The black curve in Fig. 11 suggests that the surface albedo in the calculations is biased low by about 9% (y-axis intercept of ~0.91, $y_0 = a - e^c$), whereas almost no bias is detectable in the cloud properties (a

20 of ~1.01). Figure 12 shows the fits for the spectrum between 350 and 1800nm. Two spectra are calculated: the intercept when $x = 0$ ($y_0(\lambda)$, corresponding to cloud-free conditions; and the spectrum in the limit of large x (denoted as $y_\infty(\lambda) = a$), corresponding to cloudy conditions. The $y_0(\lambda)$ spectrum (red) is consistently lower than 1.0 at short wavelengths (< 1300 nm) and slightly greater than 1.0 for wavelengths longer than 1500 nm. This suggests that the surface albedo is underestimated for the shorter wavelengths and overestimated for the longer wavelengths. Simply changing the snow fraction does not improve the agreement; it is the spec-

25 trum itself that seems to have changed somewhat over the course of two days. This is either due to physical changes of the surface, a slightly different sun angle, or instrument performance changes. The $y_\infty(\lambda)$ spectrum (blue) oscillates around 1.0 for the shorter wavelengths and is consistently larger than 1.0 for longer wavelengths, which might suggest that the retrieved effective radius is slightly biased. With these qualifications in mind, the agreement between MODIS-derived and measured irradiance is remarkable. Unfortunately, owing to limited sampling time, the below-cloud flight (13 September) leg does not lend itself to any conclusions

30 from a cloud transmittance perspective since it is not the same cloud field as on 11 September. In future flight campaigns, coordinated above- and below-cloud legs will furnish more information on bias analyses than possible from ARISE.

4 Conclusions

In this paper, we used aircraft observations to validate shortwave irradiance derived from satellite passive imagery (MODIS) of low-level cloud fields. This was done with two consecutive flights from the NASA ARISE campaign, which sampled the radiation

35 below and above a cloud field in a similar location of the MIZ. Such validation studies are especially important in the Arctic because observations from the surface are sparse. Despite their limitations, passive imagery products are one of the essential data sources for observationally-based estimates of the surface radiative flux under cloudy conditions, which necessitates a quality assessment of cloud detection and the derivation of cloud optical parameters for a variety of specific cloud and surface types as

well as surface angles. In addition, accurate knowledge of the surface albedo and of the water vapor vertical distribution is required to derive the net fluxes at the surface, above the cloud layer, and at the top of atmosphere. The two cases analyzed here only focused on one region with one specific surface and cloud type, but this allowed developing a validation approach that can help answer specific questions such as:

1. What is the reliability of passive imagery cloud detection in the MIZ and over solid snow-covered regions?
2. How much do undetected clouds bias imagery-derived irradiance, especially at the surface?
3. What is the relative magnitude of irradiance errors caused by undetected clouds, biased cloud properties, incorrect surface albedo parameterization, and water vapor?

This paper sheds some light on these questions using the combined measured broadband and spectral irradiance in the study region,
10 but these results are far from representative for the Arctic as a whole. To gain a statistically based understanding, validation data from multiple experiments will have to be combined. By aggregating data from multiple missions, it should be possible to answer more general questions, which a single case study cannot address:

● Do existing cloud climatologies from space-borne passive imagery observations accurately reproduce the frequency of low-level optically thin clouds over different surface types?

● Do existing climatologies of surface albedo capture the spatial and temporal variability sufficiently to keep errors in the derived all-sky irradiance and cloud radiative effects to an acceptable level?

It is unclear what "acceptable" would mean for the second question, but our study showed that the actual surface albedo may deviate from commonly used climatologies. Throughout the Arctic, inaccurate knowledge of the surface albedo and its variability may lead to an inaccurate estimation of cloud radiative effects and net surface fluxes, even under clear-sky conditions. This is
20 especially important in the visible part of the spectrum where most of the shortwave energy resides, and where the albedo of different surface types (ice, fresh and old snow) varies significantly. Of course, knowledge of the near-infrared variability of snow and ice albedo (via grain size) is also important because it affects the accuracy of imagery-derived cloud products.

To capture the spatial and spectral variability of the surface, we developed a data aggregation technique that combines collective measurements in a partially snow-covered environment into one spectral surface albedo dataset that is parameterized by
25 snow fraction ("binary" representation of the radiative surface properties). The dataset we obtained agrees with ground-based measurements for the two extremes (called spectral end-members): snow and thin ice. In our case, ice-free open ocean was radiatively insignificant, and the two end-members were sufficient to represent the surface variability. In more complex, more general cases, more end-members may be required.

In assessing the relative magnitude of different errors (question 3 above), we found that undetected clouds have the most
30 significant impact on the imagery-derived irradiance. In the case studied here, MODIS did not detect clouds below a threshold of 0.5 in optical thickness, even when including partially cloud-covered pixels. Undetected thin clouds (COT<0.5) led to a high bias of about 45 Wm^{-2} below clouds for the downwelling and a low bias of 19 Wm^{-2} above clouds for the upwelling shortwave irradiance – the primary error source. Secondary error sources are (a) surface albedo, and (b) cloud optical properties. By using an SSFR-derived surface albedo and atmospheric profiles from aircraft measurements and MERRA-2 along with MODIS-COPs in RTM
35 calculations, we achieved excellent agreement with the measured spectral and broadband shortwave irradiance.

While the calculations in the above-cloud case can be constrained through the TOA radiation product from satellite observations (CERES), the below-cloud calculations do not have such constraints. The attribution of the individual error contributions was done based on measurements from the SSFR, by distinguishing the different physical mechanisms based on their spectral dependence. Under some circumstances, the different errors may compensate partially in the broadband irradiance.

An overarching goal of studies such as this should be to quantify the absolute and relative magnitude of some of the errors discussed here. This will be done by analyzing more data from ARISE and other field experiments in a similar fashion as proposed here. In addition, targeted field operations will be required to systematically do so for a range of cloud types. A critical piece of such studies should be the characterization of surface properties, which are almost as important as the cloud properties themselves.

5   Generalizing the findings from airborne studies such as these will only be possible by improving satellite remote sensing along the way, which in turn requires airborne observations for the development and validation of a new generation of cloud retrievals in the Arctic. Such retrievals will need to account for surface and cloud variability, and address the issue of undetected thin clouds. A database of spectral albedos, acquired with similar techniques as proposed here, would provide the necessary testbed for developing operational space-based retrievals for surface reflectance as available for the lower latitudes. With lower COT thresholds for cloud

10   detection, spatially and temporally dependent surface albedo, accurate cloud retrievals even for thin clouds, passive remote sensing will significantly improve our current understanding of cloud radiative effects in the Arctic. Finally, it will be important to pursue a similar strategy for the thermal wavelength range.

Appendix

A. Diffuse/Direct Correction

15   The diffuse/direct correction is made under the assumption of

$$DR(\lambda) = DR_{clear}(\lambda) \cdot f + DR_{cloud}(\lambda)(1-f)$$

where DR is the "diffuse to total" ratio, f itself is the fraction of clear-sky and *(1–f)* is the fraction of an artificial diffuser (here clouds), clear indicates under clear-sky condition and cloud indicates under cloudy-sky condition.

Assume $DR_{cloud}(\lambda) = 1.0$, we get

20   $$DR(\lambda) = DR_{clear}(\lambda) \cdot f + (1-f)$$

Rearrange we get

$$DR(\lambda) = 1 - f \cdot \left(1 - DR_{clear}(\lambda)\right) \tag{1}$$

Let's denote the measured DR from SPN1, DR_{SPN1}

$$DR_{SPN1} = \frac{\int_{\lambda_1}^{\lambda_2} DR(\lambda) \cdot F^{\downarrow}(\lambda) d\lambda}{\int_{\lambda_1}^{\lambda_2} F^{\downarrow}(\lambda) d\lambda} \tag{2}$$

25   where λ_1 and λ_2 are the wavelength range of SPN1 and $F^{\downarrow}(\lambda)$ is the calculated downwelling spectral irradiance from RTM. Plug Equation (1) in (2) we get

$$DR_{SPN1} = \frac{\int_{\lambda_1}^{\lambda_2}[1 - f \cdot \left(1 - DR_{clear}(\lambda)\right)] \cdot F^{\downarrow}(\lambda) d\lambda}{\int_{\lambda_1}^{\lambda_2} F^{\downarrow}(\lambda) d\lambda}$$

Rearrange we get

$$DR_{SPN1} = 1 - f \cdot \frac{\int_{\lambda_1}^{\lambda_2} F^{\downarrow}(\lambda) \cdot \left(1 - DR_{clear}(\lambda)\right) d\lambda}{\int_{\lambda_1}^{\lambda_2} F^{\downarrow}(\lambda) d\lambda} \tag{3}$$

30   Then

$$f = \frac{1 - DR_{SPN1}}{\left. \int_{\lambda_1}^{\lambda_2} F_{clear}^{\downarrow}(\lambda) \cdot \left(1 - DR_{clear}(\lambda)\right) d\lambda \middle/ \int_{\lambda_1}^{\lambda_2} F_{clear}^{\downarrow}(\lambda) d\lambda \right.}$$

Then

$$DR(\lambda) = DR_{clear}(\lambda) \cdot f + (1 - f)$$

5 **B. Azimuth Response**

Since SSFR only covers part of BBR's bandwidth from 200 to 3600 nm, RTM calculations were used to fill in SSFR spectra beyond its nominal wavelength range of 350 – 2050 nm. Subsequently, the SSFR spectral irradiance was spectrally integrated (referred to as F_{SSFR}). A second-order Fourier series was applied to fit the azimuthal dependence captured by F_{SSFR}/F_{BBR}. Fig. 13 shows the ratio (F_{SSFR}/F_{BBR}) as a function of reference azimuth angle, defined as the azimuth angle of the sun with respect to the

10 light collector, 0 degrees defined as the aircraft flying towards to the North. A second-order Fourier series was applied to fit the azimuthal dependence captured by F_{SSFR}/F_{BBR}. It constitutes SSFR's azimuthal response at this solar zenith angle, which was then used to correct SSFR's downwelling irradiance for the conditions encountered for the SSFR data collected during other research flights.

C. Adaptive Thresholding

The threshold value at each pixel location of the image depends on the neighboring pixel intensities I. For a pixel located at (x, y), the threshold value $T(x, y)$ is calculated through the following steps:

1. A subdomain of $d \times d$ is selected with (x, y) at the center of the subdomain;

20 2. The weighted average $C(x, y)$ is calculated for the subdomain using Gaussian weights (Davies 1990) $W(x, y)$, $C(x, y) = \sum_{i=0}^{d} \sum_{j=0}^{d} I(i, j) \cdot W(i, j)$;

3. The threshold for the pixel at (x, y) is the difference of the weighted average calculated in the previous step and a constant C_0, $T(x, y) = C(x, y) - C_0$.

d and C_0 are input parameters that can be adjusted to improve the results. In this study, the d is set to 1501 and C_0 is set to 0.

Acknowledgements. This work was supported by NASA grants NNX12AC11G (SSFR data collection during ARISE) and NNX14AP72G (data analysis). MODIS data were provided by the NASA/Goddard Space Flight Center's Level-1 and Atmosphere Archive and Distribution System (LAADS) (http://dx.doi.org/10.5067/MODIS/MOD06_L2.061).

References

5 Anderson, G. P., Clough, S. A., Kneizys, F. X., Chetwynd, J. H., and Shettle, E. P.: AFGL atmospheric constituent profiles (0 - 120km). Tech. Rep. AFGL-TR-86–0110, (954), 46, 1986.

Badosa, J., Wood, J., Blanc, P., Long, C. N., Vuilleumier, L., Demengel, D., and Haeffelin, M.: Solar irradiances measured using SPN1 radiometers: Uncertainties and clues for development, Atmos. Meas. Tech., 7(12), 4267–4283, doi:10.5194/amt-7-4267-2014, 2014.

10 Bannehr, L., and Schwiesow, R.: A technique to account for the misalignment of pyranometers installed on aircraft, J. Atmos. Ocean. Tech., 10, 774–777, 1993.

Bennartz, R., Shupe, M. D., Turner, D. D., Walden, V. P., Steffen, K., Cox, C. J., Kulie, . S., Miller, N.B., and Pettersen, C.: July 2012 Greenland melt extent enhanced by low-level liquid clouds. Nature, 496, 83–86, 2013.

Bosilovich, M., and Coauthors: MERRA-2: Initial evaluation of the climate. NASA Tech. Rep. Series on Global Modeling and 15 Data Assimilation NASA/TM-2015-104606, 2015

Brandt, R. E., Warren, S. G., Worby, A. P., and Grenfell, T. C.: Surface albedo of the Antarctic sea ice zone, J. Climate, 18, 3606–3622, 2005.

Bucholtz, A., Bluth, R. T., Kelly, B., Taylor, S., Batson, K., Sarto, A. W., Tooman, T P., and McCoy, Jr., R. F.: The Stabilized Radiometer Platform (STRAP) - An actively stabilized horizontally level platform for improved aircraft irradiance measure-20 ments, J. Atmos. Ocean. Tech, 25, 2161–2175, 2008.

Bucholtz, A., Hlavka, D. L., McGill, M. J., Schmidt, K. S., Pilewskie, P., Davis, S. M., Reid, E. A., and Walker, A. L.: Directly Measured Heating Rates of a Tropical Subvisible Cirrus Cloud, J. of Geophys. Res., 115, 1-11, 2010.

Curry, J. A., Schramm, J. L., Serreze, M. C., and Ebert, E. E.: Water vapor feedback over the Arctic Ocean, J. Geophys. Res., 100, 14223–14229, 1995.

25 Curry, J. A., Rossow, W. B., Randall, D., and Schramm, J. L.: Overview of arctic cloud and radiation characteristics, J. Climate, 9, 1731–1764, 1996.

Davies, E. R.: Machine Vision: Theory, Algorithms, Practicalities, 3rd Edition, Elsevier, Inc., 934 pp., 2005.

Doyle, J. G., Lesins, G., Thackray, C. P., Perro, C., Nott, G. J., Duck, T. J., Damoah, R., and Drummond, J. R.: Water vapor intrusions into the High Arctic during winter, Geophys, Res, Lett,, 38, L12806, doi:10.1029/2011GL047493, 2011.

30 Emde, C., Buras-Schnell, R., Kylling, A., Mayer, B., Gasteiger, J., Hamann, U., Kylling, J., Richter, B., Pause, C., Dowling. T. and Bugliaro, L.: The libRadtran software package for radiative transfer calculations (version 2.0.1), Geosci. Model Develop., 9, 1647–1672, doi:10.5194/gmd-9-1647-2016, 2016.

Gonzalez, R. C., Woods, R. E., and Eddins, S. L.: Image Segmentation. Digital Image Processing, 600–603, 2002.

Haeberli, P., and Voorhies, D.: Image processing by linear interpolation and extrapolation, IRIS Universe Magazine, 28, 8–9, 1994.

35 Hartmann, D. L., and Ceppi, P.: Trends in the CERES dataset, 2000-13: The effects of sea ice and jet shifts and comparison to climate models, J. Climate, 27, 2444–2456, 2014.

Henderson, D. S., L'Ecuyer, T., Stephens, G., Partain, P., and Sekiguchi, M.: A multisensor perspective on the radiative impacts of clouds and aerosols, J. Appl. Meteorol. Clim., 52, 853–871, 2013.

Kay, J. E., and L'Ecuyer, T.: Observational constraints on Arctic Ocean clouds and radiative fluxes during the early 21st century, J. Geophys. Res., 118, 7219–7236, 2013.

Kindel, B. C.: Cloud shortwave spectral radiative properties: Airborne hyperspectral measurements and modeling of irradiance, Ph.D. Dissertation, University of Colorado Boulder, United States, 130 pp., 2010.

5   King, M. D., Platnick, S., Yang, P., Arnold, G. T., Gray, M. A., Riedi, J. C., Ackerman, S. A., and Liou, K. N.: Remote sensing of liquid water and ice cloud optical thickness and effective radius in the Arctic: Application of airborne multispectral MAS data, J. Atmos. Ocean. Tech, 21, 857–875, 2004.

Kurucz, R. L.: Synthetic infrared spectra, In Infrared Solar Physics, Rabin, D. M., Jefferies, J. T., and Lindsey, C. (Eds.), Springer-Science+Business Media, B. V., 523–531, 1992.

10 Lyapustin, A., Gatebe, C. K., Kahn, R., Brandt, R., Redemann, J., Russell, P., King, M. D., Pedersen, C. A., Gerland, S., Poudyal, R., Marshak, A., Wang, Y., Schaaf, C., Hall, D., and Kokhanovsky, A.: Analysis of snow bidirectional reflectance from ARCTAS Spring-2008 campaign, Atmos. Chem. Phys., 10, 4359–4375, 2010.

Liu, Y., Ackerman, S. A., Maddux, B. C., Key, J. R., and Frey, R. A.: Errors in cloud detection over the arctic using a satellite imager and implications for observing feedback mechanisms, J. Climate, 23, 1894–1907, 2010.

15 Loeb, N. G., and Manalo-Smith, N.: Top-of-atmosphere direct radiative effect of aerosols over global oceans from merged CERES and MODIS observations, J. Climate, 18, 3506–3526, 2005.

Loeb, N. G., Kato, S., Su, W., Wong, T., Rose, F. G., Doelling, D. R., Norris, J. R., and Huang, X.: Advances in understanding top-of-atmosphere radiation variability from satellite observations, Surv. Geophys., 33, 359–385, 2012.

Long, C. N., Bucholtz, A., Jonsson, H., Schmid, B., Vogelmann, A., and Wood, J.: A method of correcting for tilt from horizontal in downwelling shortwave irradiance measurements on moving platforms, The Open Atmos. Sci. J., 4, 78–87, 2010.

20 Moody, E. G., King, M. D., Schaaf, C. B., Hall, D. K., and Platnick, S.: Northern Hemisphere five-year average (2000-2004) spectral albedos of surfaces in the presence of snow: Statistics computed from Terra MODIS land products, Remote Sens. Environ., 111, 337–345, 2007.

Nakajima, T., and King, M. D.: Determination of the optical thickness and effective particle radius of clouds from reflected solar radiation measurements. Part I: Theory, J. Atmos. Sci., 47, 1878–1893, 1990.

25 Oreopoulos, L., Cho, N., Lee, D., and Kato, S.: Radiative effects of global MODIS cloud regimes, J. Geophys. Res., 121, 2299–2317, 2016.

Perovich, D. K.: Seasonal evolution of the albedo of multiyear Arctic sea ice, J. Geophys. Res., 107(C10), 8044, doi: 10.1029/2000JC000438, 2002.

30 Pierluissi, J. H., and Peng, G. : New molecular transmission band models for LOWTRAN, Optical Engineering, 24, 541–547, doi: 10.1117/12.7973523, 1985.

Pilewskie, P., Pommier, J., Bergstrom, R., Gore, W., Howard, S., Rabbette, M., Schmid, B., Hobbs, P. V., and Tsay, S. C.: Solar spectral radiative forcing during the Southern African Regional Science Initiative, J. Geophys. Res., 108(D13), 8486, doi:10.1029/2002JD002411, 2003.

35 Platnick, S., Li, J. Y., King, M. D., Gerber, H., and Hobbs, P. V.: A solar reflectance method for retrieving the optical thickness and droplet size of liquid water clouds over snow and ice surfaces, J. Geophys. Res., 106, 15185–15199, 2001.

Platnick, S., King, M. D., Ackerman, S. A., Menzel, W. P., Baum, B. A., Riédi, J. C., and Frey, R. A.: The MODIS cloud products: Algorithms and examples from Terra, IEEE Trans. Geosci. Remote Sens., 41, 459–473, 2003.

Platnick, S., Ackerman, S. A., King, M. D., Wind, G., Meyer, K., Menzel, W. P., Frey, R. A., Holz, R. E., Baum, B. A., and Yang,
40   P.: MODIS Atmosphere L2 Cloud Product (06_L2). NASA MODIS Adaptive Processing System, Goddard Space Flight

Center, USA, http://dx.doi.org/10.5067/MODIS/MOD06_L2.006, 2017.

Platnick, S., Meyer, K. G., King, M. D., Wind, G., Amarasinghe, N., Marchant, B., Arnold, G. T., Zhang, Z., Hubanks, P. A., Holz, R. E., and Yang, P.: The MODIS cloud optical and microphysical products: Collection 6 updates and examples from Terra and Aqua, IEEE Trans. Geosci. Remote Sens., 55, 502-525, 2017.

5 Schmidt, G. A., Ruedy, R. A., Miller, R. L., and Lacis, A. A.: Attribution of the present-day total greenhouse effect, J. Geophys. Res., 115, D20106, doi:10.1029/2010JD014287, 2010.

Rozenhaimer, M., Barton, N., Redemann, J., Schmidt, S., LeBlanc, S., Anderson, B., Winstead, E., Corr, C. A., Moore, R., Thornhill, K. L., and Cullather, R. I.: Bias and sensitivity of boundary layer clouds and surface radiative fluxes in MERRA-2 and airborne observations over the Beaufort Sea during the ARISE campaign, J. Geophs. Res. Atmos., 123, doi: 10 10.1029/2018JD028349.

Schmidt, S., and Pilewskie, P.: Airborne measurements of spectral shortwave radiation in cloud and aerosol remote sensing and energy budget studies, In A. A. Kokhanovsky (Ed.), Light Scattering Reviews, Vol. 6: Light Scattering and Remote Sensing of Atmosphere and Surface, Berlin, Heidelberg: Springer Berlin Heidelberg, 239–288, doi:10.1007/978-3-642-15531-4_6, 2012.

15 Sedlar, J., and Devasthale, A.: Clear-sky thermodynamic and radiative anomalies over a sea ice sensitive region of the Arctic, J. Geophys. Res., 117, D19111, doi:10.1029/2012JD017754, 2012.

Shupe, M. D., Walden, V. P., Eloranta, E., Uttal, T., Campbell, J. R., Starkweather, S. M., and Shiobara, M.: Clouds at Arctic atmospheric observatories. Part I: Occurrence and macrophysical properties, J. Appl. Meteorol. Clim., 50, 626–644, 2011.

Shupe, M. D., and Intrieri, J. M.: Cloud radiative forcing of the Arctic surface: The influence of cloud properties, surface albedo, 20 and solar zenith angle, J. Climate, 17, 616–628, 2004.

Smith, W. L., Hansen, C., Bucholtz, A., Anderson, B. E., Beckley, M., Corbett, J. G., Cullather, R. I., Hines, K.M., Hofton, M., Kato, S., Lubin, D., Moore, R. H., Segal Rosenhaimer, M., Redemann, J., Schmidt, S., Scott, R., Song, S., Barrick, J. D., Blair, J.B., Bromwich, D. H., Brooks, C., Chen, G., Cornejo, H., Corr, C. A., Ham, S., Kittelman, A. S., Knappmiller, S., LeBlanc, S., Loeb, N. G., Miller, C., Nguyen, L., Palikonda, R., Rabine, D., Reid, E. A., Richter-Menge, J. A., Pilewskie, P., 25 Shinozuka, Y., Spangenberg, D., Stackhouse, P., Taylor, P., Thornhill, K. L., van Gilst, D., and Winstead, E.: Arctic Radiation-IceBridge Sea and Ice Experiment: The Arctic radiant energy system during the critical seasonal ice transition. Bull. Amer. Meteor. Soc., 98, 1399–1426, https://doi.org/10.1175/BAMS-D-14-00277.1, 2017

Stamnes, K., Tsay, S.-C., Wiscombe, W., and Jayaweera, K.: Numerically stable algorithm for discrete-ordinate-method radiative transfer in multiple scattering and emitting layered media, Appl. Opt., 27, 2502–2509, 1988.

30 Warren, S. G., Roesler, C. S., and Brandt, R. E.: Solar radiation processes in the east Antarctic sea-ice zone. Antarctic J. United States, 32, 185–186, 1997.

Wendisch, M., Müller, D., Schell, D., and Heintzenberg, J.: An airborne spectral albedo meter with active horizontal stabilization, J. Atmos. Ocean. Tech, 18, 1856–1866, 2001.

Wielicki, B. A., Barkstrom, B. R., Harrison, E. F., Lee III, R. B., Smith, G. L., and Cooper, J. E.: Clouds and the Earth's Radiant 35 Energy System (CERES): An Earth Observing System Experiment. Bull. Amer. Meteor. Soc., 77, 853–868, 1996.

Wiscombe, W. J., and Warren, S. G.: A model for the spectral albedo of snow. I: Pure snow, J. Atmos. Sci., 37, 2712–2733, 1981.

Table 1. Mean of the broadband downwelling, upwelling, net, and estimated cloud radiative effect (CRE) of SSFR, BBR, RTM calculations, RTM calculations when clouds are detected, and RTM calculations when clouds are undetected (clear-sky) for September 11, 2014.

	SSFR	BBR	RTM (clouds detected)	RTM (clouds undetected)	RTM
Downwelling	402.93	399.52	407.60	405.08	406.48
Upwelling	265.52	266.66	271.66	229.23	252.82
Net	137.41	132.86	135.94	175.85	153.66
CRE	-38.44	-42.99	-39.91		

Table 2. Same as Table 1 except for September 13, 2014.

	SSFR	BBR	RTM (clouds detected)	RTM (clouds undetected)	RTM
Downwelling	210.17	211.90	210.70	329.50	256.26
Upwelling	162.71	162.49	163.99	244.07	194.70
Net	47.46	49.41	46.71	85.43	61.56
CRE	-37.97	-36.02	-38.72		

11 September 13 September
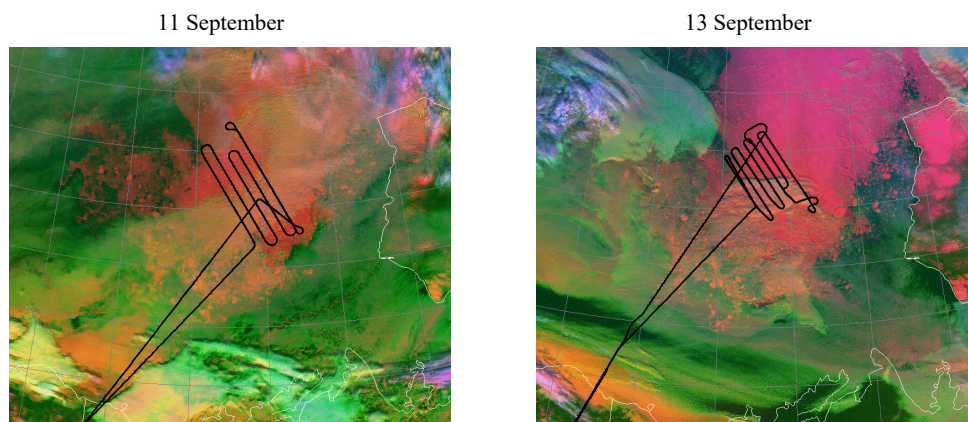
Figure 1. ARISE flight tracks overlaid on MODIS false color imagery (0.65 *µm* for red, 11 *µm* for blue, and 3.7-11 *µm* for green) from NASA Langley Research Center on 11 September and 13 September 2014.
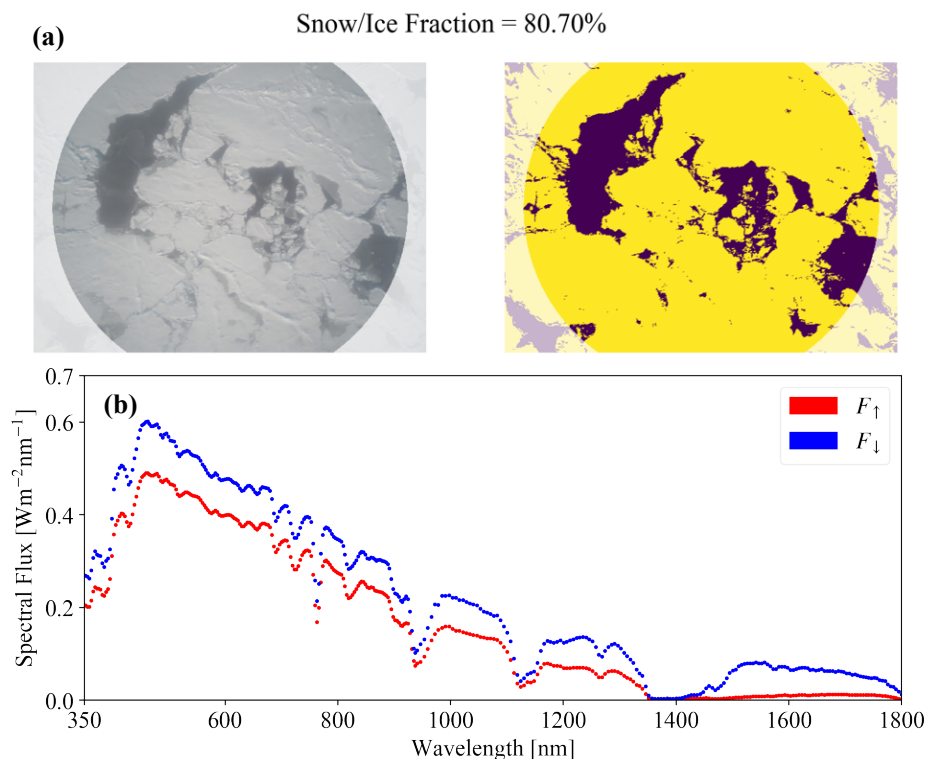
5 **Figure 2**. **(a)** An example of snow fraction estimated from nadir camera imagery at 20:03:32 UTC on 13 September. The left panel is the nadir camera imagery. The right panel uses yellow and purple to indicate bright and dark pixels detected by the adaptive thresholding method. The snow fraction is derived from the abundance of yellow pixels. **(b)** The upwelling and downwelling irradiance measured by SSFR at the same time.
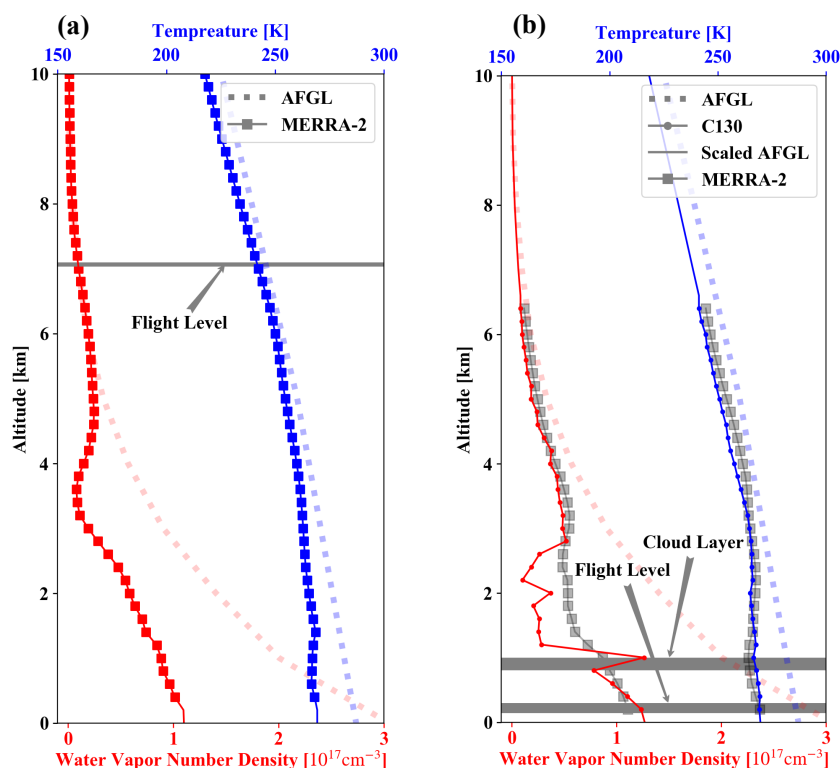
Figure 3. Vertical profiles of temperature and water vapor from MERRA-2 for (a) 11 September and (b) from C130 for 13 September 2014. On 11 September, the cloud location is unavailable from in-situ data. Based on the temperature inversion location, it is likely below 1.0-1.5 km.
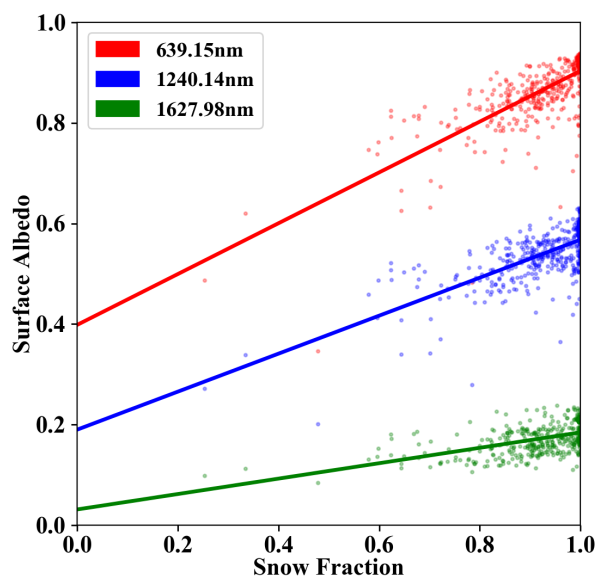
Figure 4. Estimated snow fraction from nadir imagery versus SSFR measured surface albedo at 640 nm, 1240 nm, and 1630 nm.

Linear regression fits are indicated by the solid lines.
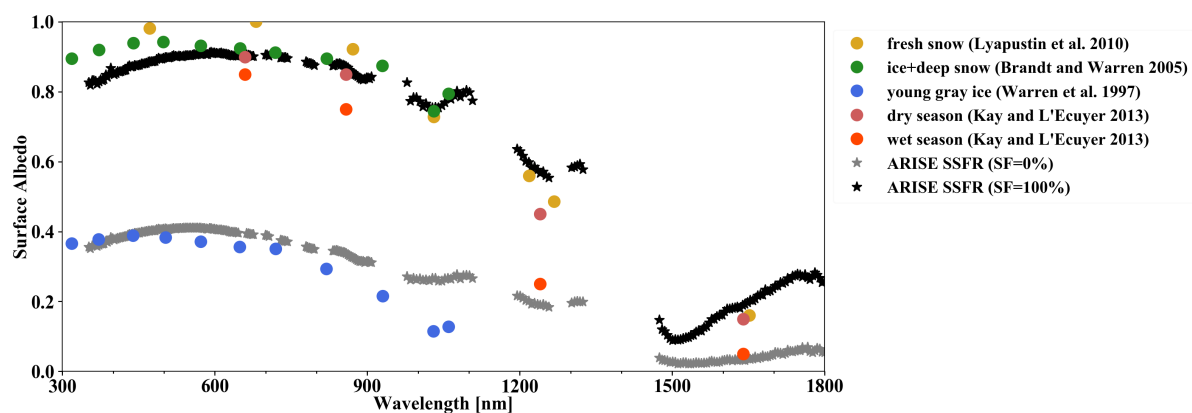
Figure 5: Spectral surface albedo derived from SSFR measurements for 100% snow fraction and 0 snow fraction.
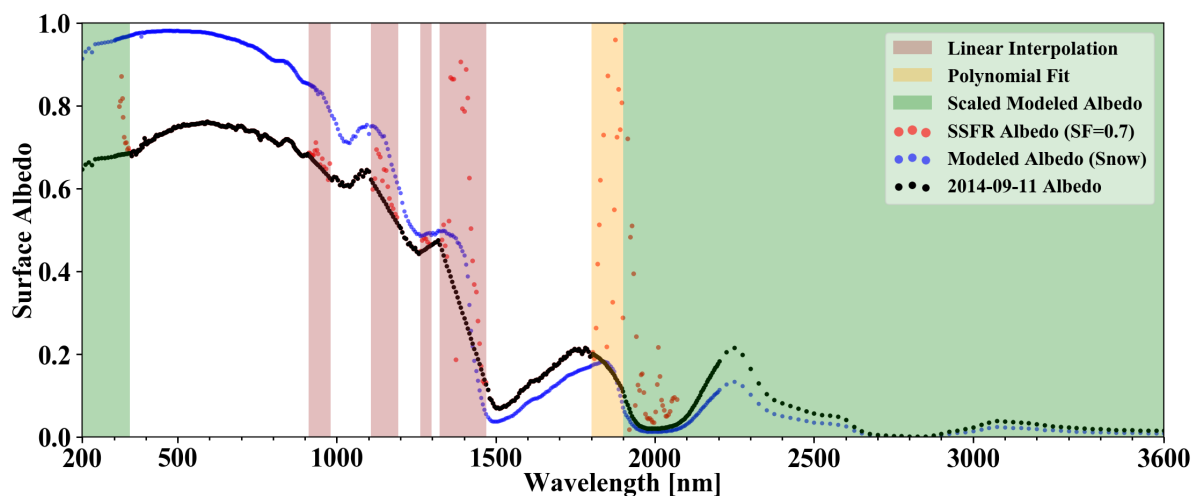
Figure 6: Spectral surface albedo (black) used in RTM for 2014-09-11 irradiance calculations. The spectral albedo uses the SSFR-derived albedo with a snow fraction of 0.7 (red) except the wavelength ranges marked in green (less than 350nm and greater than 1900nm): scaled modeled snow albedo (blue); in red (gas absorption bands): linear interpolation; and in yellow (1800nm to 1900nm): polynomial fit using SSFR-derived albedo from 1650nm to 1800nm.
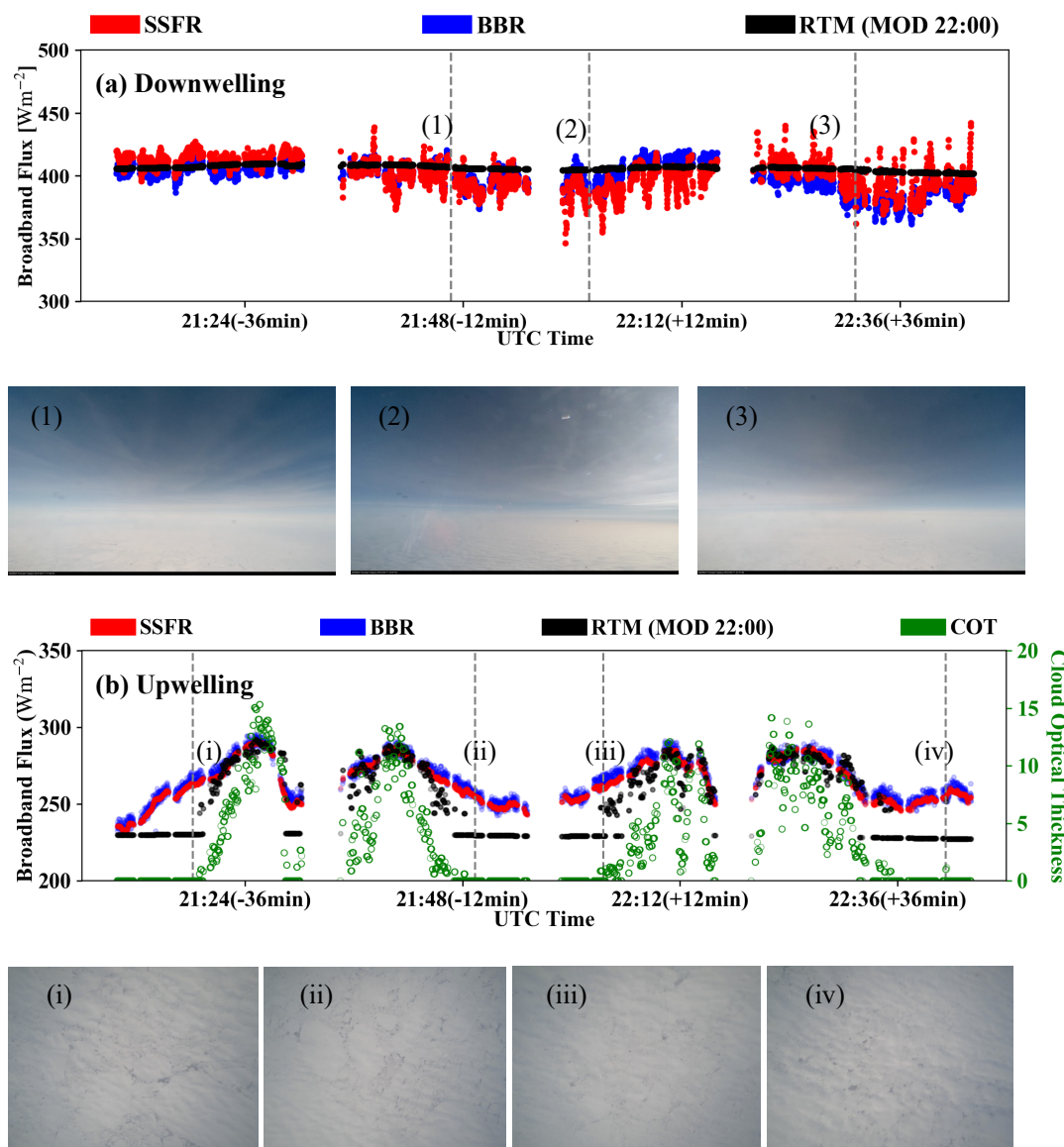
Figure 7. Broadband (a) downwelling and (b) upwelling irradiance from SSFR, BBR, and MODIS-COPs (Terra MODIS at 22:00) based RTM calculations on 11 September (above-clouds). The forward camera images are provided at (1) 21:46:39, (2) 22:01:53, and (3) 22:31:05. The nadir camera images are provided at (i) 21:18:15, (ii) 21:49:22, (iii) 22:03:28, and (iv) 22:41:18 UTC. The time differences between aircraft measurements and MODIS granule are indicated in the axis labels.
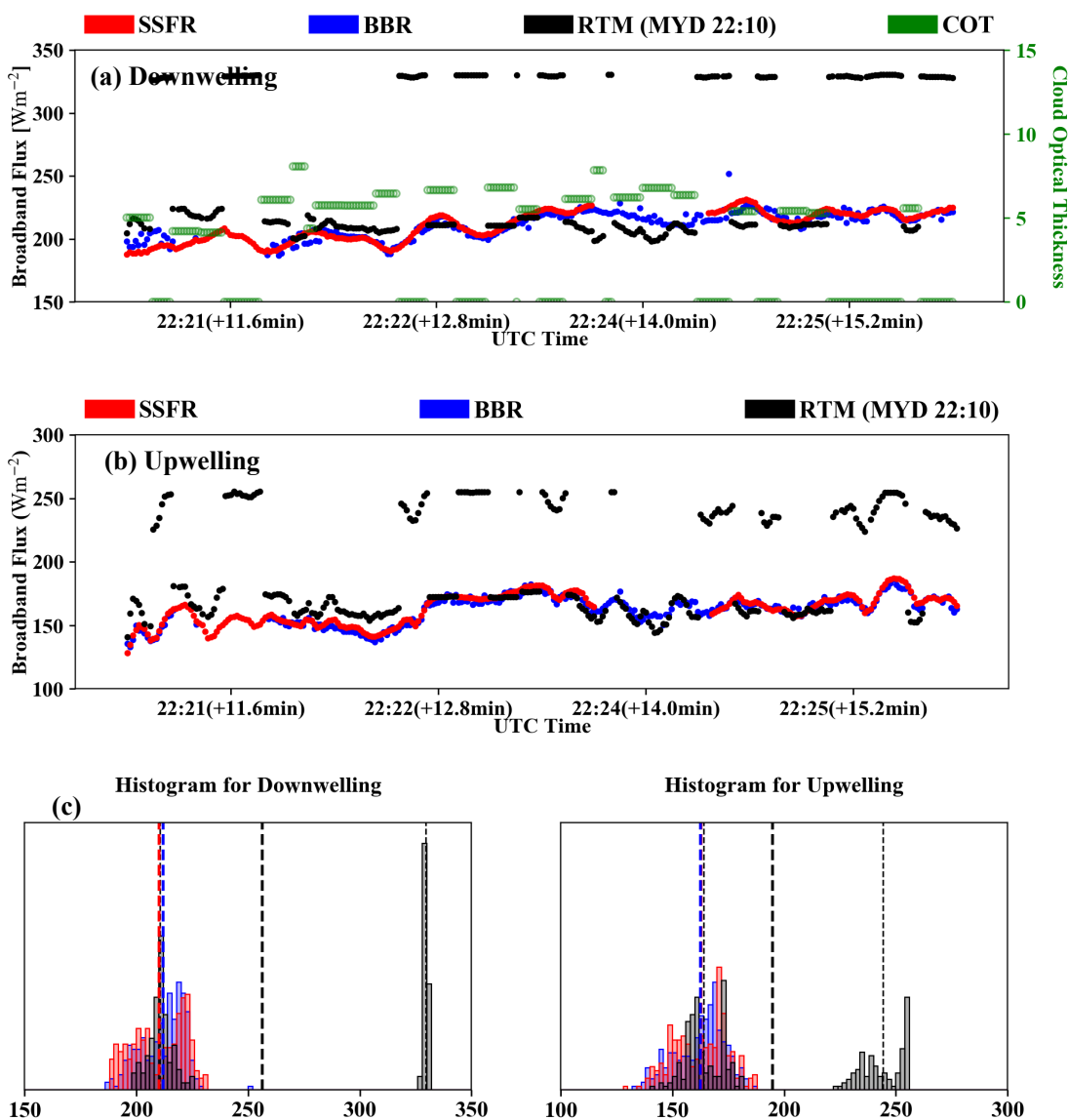
Figure 8. Broadband (a) downwelling and (b) upwelling irradiance from SSFR, BBR, and MODIS-COPs (Aqua MOODIS at

5   22:10) based RTM calculations on 13 September (below-clouds) and (c) the histograms. The time difference between aircraft

measurements and MODIS granule is indicated in the axis labels. In the histograms, the mean of BBR, SSFR, and RTM calculations

are indicated by the thick dashed lines. In addition, the mean is calculated for each of the two modes in RTM calculations and

indicated by the thin dashed lines.
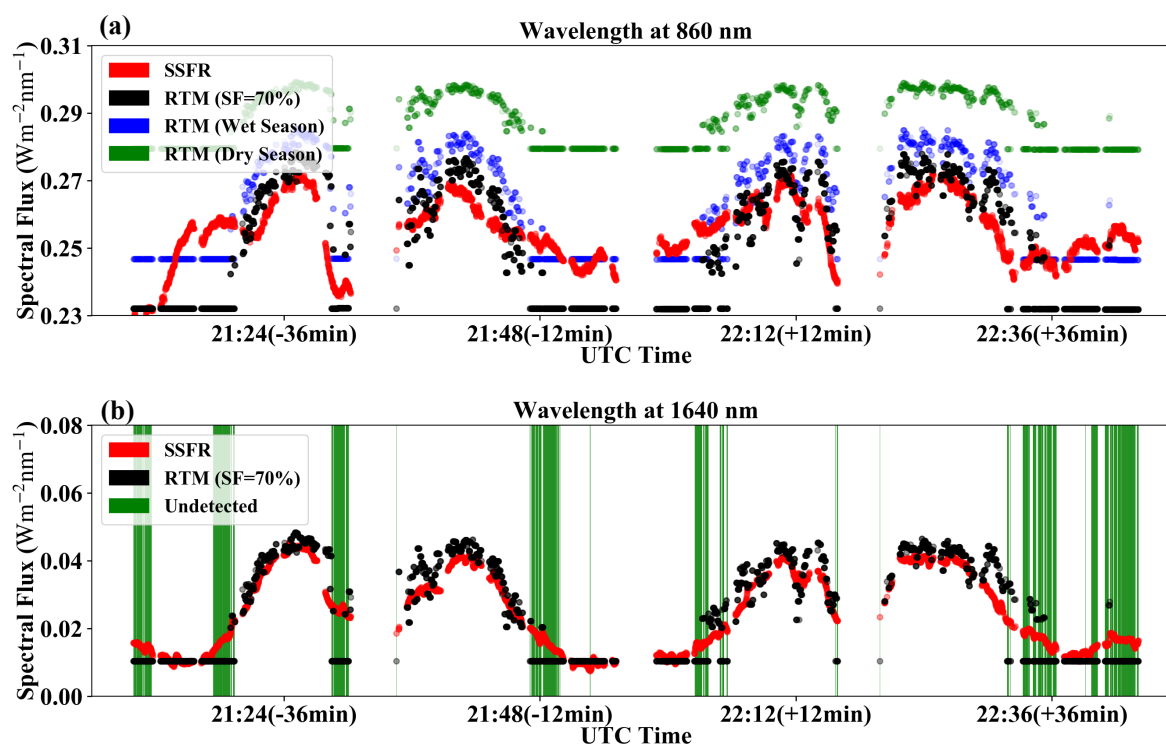
Figure 9. Spectral upwelling irradiance at 860nm (panel a) and 1640nm (panel b) from SSFR (red) and MODIS-COPs based RTM

calculations using "13 September surface albedo" with snow fraction of 70% (black) on 11 September. In addition, MODIS-COPs

based RTM calculations with climatological snow albedo of Arctic wet season (=0.75) and Arctic dry season (=0.75) are provided

for wavelength 860nm in panel (a).   The data points where the clouds were undetected are marked in green in panel (b).
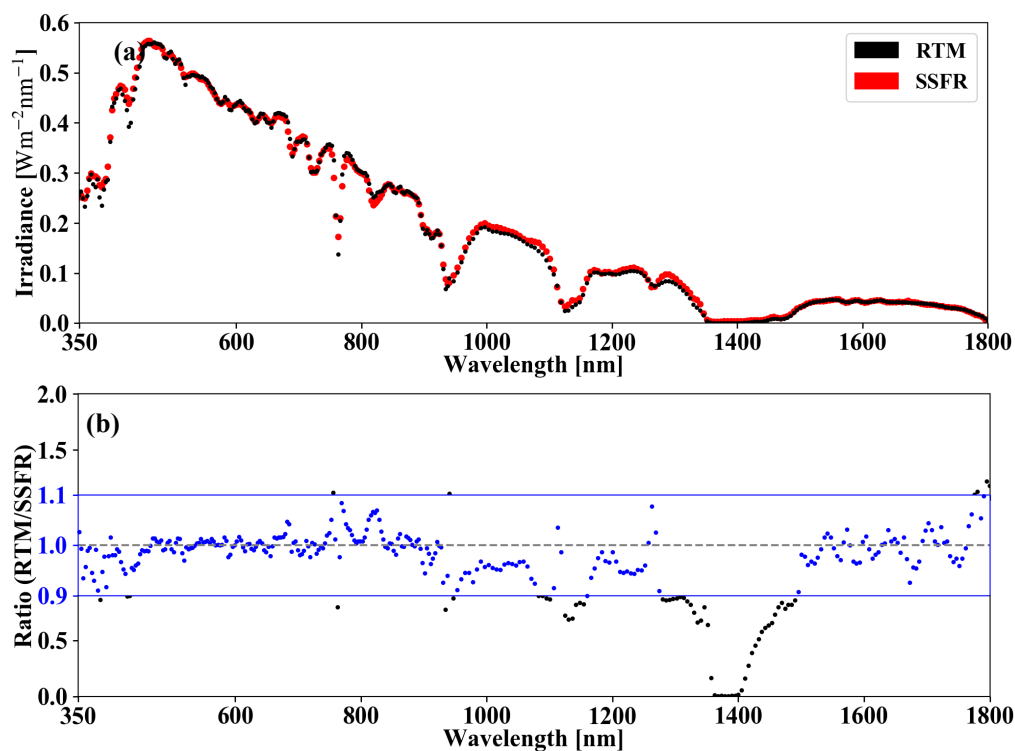
5 **Figure 10.** (a) Spectral upwelling irradiance from SSFR (red) and MODIS-COPs based RTM calculations (black) at 21:24 UTC on 11 September. (b) Spectral ratio (RTM/SSFR) of (a). The ratio with values between 0.9 and 1.1 is zoomed in and color-coded in blue.
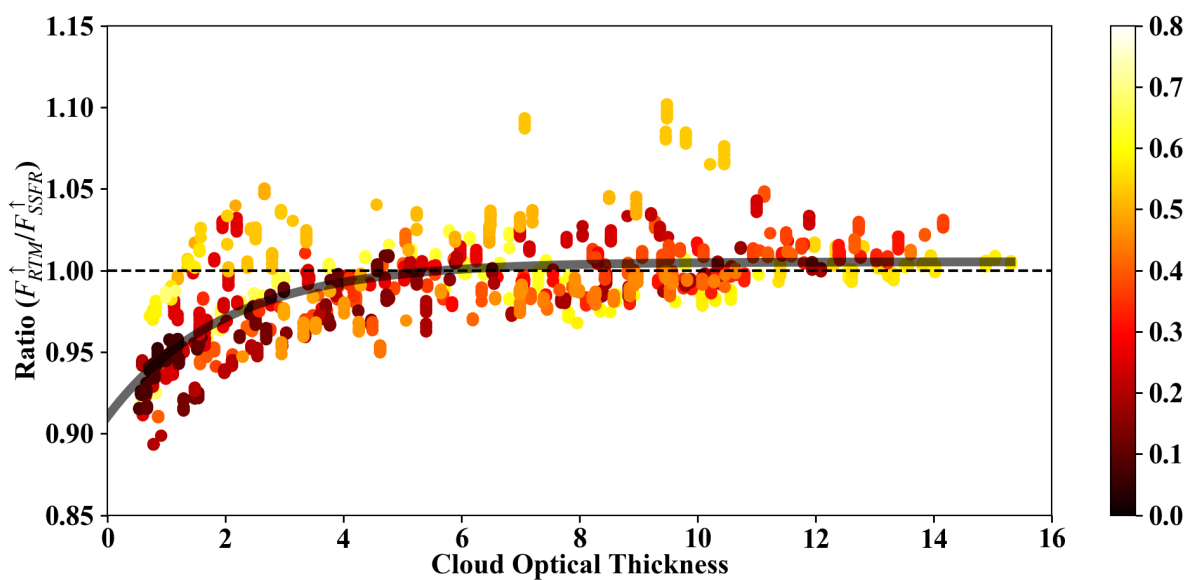
Figure 11. Ratio (RTM/SSFR) of upwelling broadband irradiance as a function of cloud optical thickness from MODIS "1621" cloud product on 11 September. The time differences between aircraft measurements and MODIS granule (unit: hour) is color-coded. The black curve is an exponentially fitted line using $y = a - e^{bx+c}$, where $a = 1.0050$, $b = -0.5027$, and $c = -2.3343$.
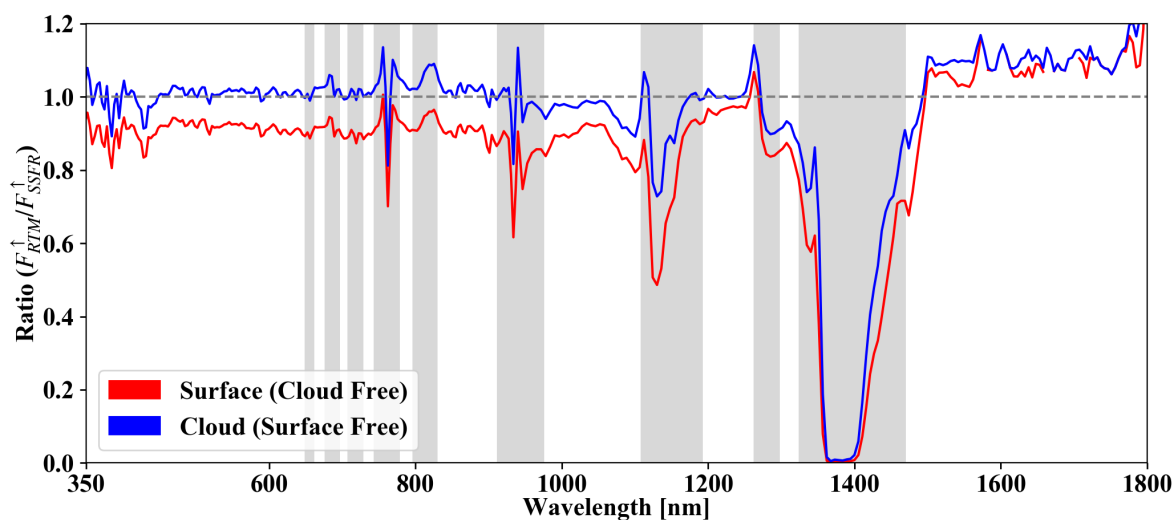
Figure 12. The intercept value of exponential fitting ($y = a - e^{bx+c}$ when $x = 0$, red, indicating cloud free) and stable value of exponential fitting ($y = a - e^{bx+c}$ when $x = 10000$, blue, indicating surface free) for all the wavelengths. The gas absorption bands are indicated in gray.
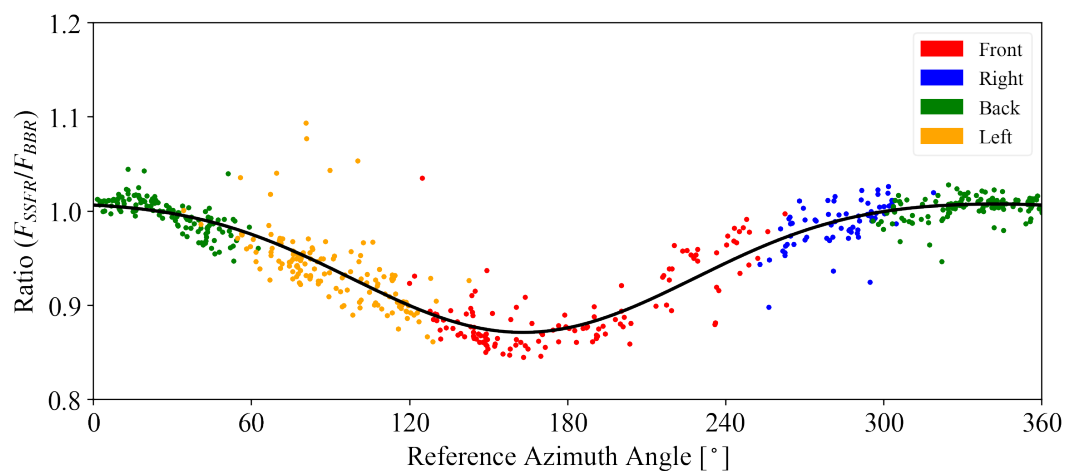
Figure 13: Ratio between spectrally integrated SSFR irradiance and broadband solar BBR irradiance as a function of reference azimuth angle (solar azimuth position with respect to the sensor, 0 degree pointing north) during 1:00 UTC – 1:36 UTC on 2014-10-03. The relative positions of the sun with respect to the aircraft are indicated by different colors. The black curve is a fitted function using a second order Fourier series.